Defect Fluorite Superstructures in the Bi_2O_3–WO_3 System

Wuzong Zhou

IRC in Superconductivity, University of Cambridge, Madingley Road, Cambridge CB3 OHE, United Kingdom

The compositional range from Bi_2O_3 to $Bi_2W_2O_9$ in the Bi_2O_3–WO_3 ternary oxide system has been investigated by X-ray powder diffraction and high-resolution electron microscopy. With very low content of WO_3, a β-Bi_2O_3-like solid solution was produced. In most compositions, $Bi_{2-x}W_xO_{3+1.5x}$, three solid solution ranges with $0.064 \le x \le 0.134$ (type Ia), $0.134 < x < 0.286$ (type Ib), and $0.286 < x < 0.364$ (type II) were identified. The structures of these solid solution materials were found to be $\sqrt{10}/2 \times \sqrt{10}/2 \times 3$ (Ia), $\sqrt{5} \times \sqrt{5} \times 2$ (Ib), and $3 \times 3 \times$ (II) superstructures based on fluorite-like δ-Bi_2O_3. Structural models with the typical compositions of $Bi_{14}WO_{24}$, $Bi_{14}W_2O_{27}$, and $Bi_{92}W_{16}O_{186}$ have been proposed. The mechanisms of formation of the superstructures and the phase transitions governed by oxygen vacancies are discussed. © 1994 Academic Press, Inc.

INTRODUCTION

It is known that the high-temperature phase of Bi_2O_3 (δ-type) (1), which has a defect fluorite-like *fcc* unit cell with $a = 5.6$ Å, can be stabilized at room temperature by chemical substitution using many other metal oxides. Ternary oxides in the Bi_2O_3–Nb_2O_5 (2–4), Bi_2O_3–Ta_2O_5 (5), and Bi_2O_3–V_2O_5 (6, 7) systems have been investigated previously by high-resolution electron microscopy (HREM). Although X-ray powder diffraction (XRD) patterns from a wide range of composition in each of these systems indicated only the δ-Bi_2O_3-like structure, many superstructures were observed in the HREM studies. When the contents of the guest oxides were very low in the Bi_2O_3–M_2O_5 systems, metastable high-temperature phases, β-Bi_2O_3- ($M = $ Nb or Ta) and γ-Bi_2O_3-related ($M = $ V) solid solutions, were produced. However, increasing the concentrations of the guest oxides leads to the δ-Bi_2O_3-like solid solutions, in which the guest cations existed in some ordered or partially ordered clusters, forming various superstructures. The type I superstructure contains isolated MO_6 ($M = $ Nb or Ta) octahedra or VO_4 tetrahedra. The characteristic feature in the type II superstructures is a formation of Nb_4O_{18}, Ta_4O_{18}, or V_4O_{10} tetrahedral clusters in the δ-Bi_2O_3 matrix. The more complicated type III (4, 5) and type IV (8) superstructures

containing perovskite-like M_4O_{20} ($M = $ Nb or Ta) square units were also observed. Physicochemical properties of these solid solution materials were found to depend on the formation of these clusters (9, 10).

In pure δ-Bi_2O_3, 25% of anion positions are unoccupied. It was assumed that the oxygen vacancies played an important role in the phase transitions in the Bi_2O_3-containing ternary oxide systems, and high charge valances (5+ or 6+) of the guest cations were essential to stabilize the δ-Bi_2O_3 structure. Accordingly, WO_3 must be a better candidate for the second oxide than Nb_2O_5 and Ta_2O_5 since the W^{6+} cation, with an ionic radius (0.62 Å) similar to those of Nb^{5+} (0.69 Å) and Ta^{5+} (0.68 Å), has a higher charge valence and therefore can introduce more oxygen atoms into the anion vacancies in the δ-Bi_2O_3 structure.

Previous studies of the phase chemistry in the Bi_2O_3–WO_3 system have yielded widely differing results (Fig. 1). In 1943, Sillen and Lundborg found five phases, $Bi_{38}W_2O_{63}$, Bi_6WO_{12}, $Bi_{10}W_2O_{21}$, $Bi_6W_4O_{21}$, and $Bi_2W_3O_{12}$ (11). All of these phases were assumed to have constant compositions or at least exist over very narrow homogeneous ranges. The unit cells of some Bi-rich compositions were found to be *fcc* with the lattice constants, a, about 5.5 Å. In 1962, Smolyaninov and Belyaev investigated this system as a binary component of the ternary system of Bi_2O_3–WO_3–PbO (12). They only found three congruent compounds, Bi_6WO_{12}(I), Bi_2WO_6(II), and $Bi_2(WO_4)_3$ (III). The solid solutions of **I** with **II** and of **II** with **III** passed through minima at 988 and 830°C corresponding to 35 and 71.5 mole% WO_3, respectively. The third systematic study of this system was performed by Gal'perin *et al.* in 1966 (13). Using the XRD method, they found that the system contained a stable compound Bi_2WO_6 with a homogeneous zone that extended to the composition $Bi_{10}W_7O_{36}$ and two phases of variable compositions, $(Bi_2W_3O_{12}) + (Bi_2W_2O_9)$ and $(Bi_4WO_9) + (Bi_{10}WO_{18})$, in which an order–disorder transition was possible. Stabilization of δ-Bi_2O_3 at room temperature was possible on introduction of 9% WO_3. At the lowest WO_3 content, β-Bi_2O_3 was stabilized. In 1970, Speranskaya (14) reported five compounds with the elemental ratio, Bi : W, of 12 : 1,
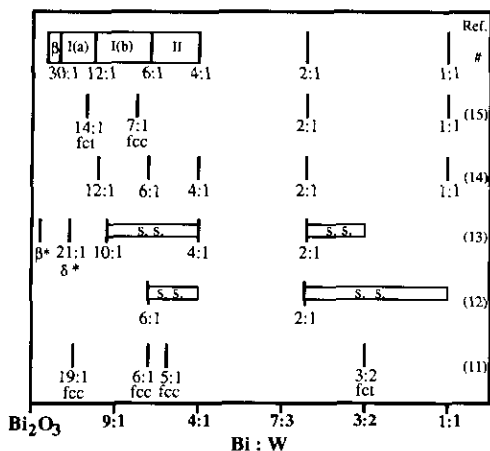
FIG. 1. The previous and present (marked by #) phase identifications of the Bi_2O_3-WO_3 system in the compositional range from Bi_2O_3 to $Bi_2W_2O_9$. The ratios of Bi : W are indicated. S.S. represents solid solution.

TABLE 1
Specimen Preparations

Starting composition (Bi : W)	Heating temperature (°C)	Initial time (hr)	Main phase present (type)
60 : 1	820	144	β-type
30 : 1	820	144	Ia
19 : 1	820	100	Ia
14 : 1	830	115	Ia
12 : 1	830	115	Ia, Ib
9 : 1	825	96	Ib
7 : 1	900	96	Ib
6 : 1	900	96	Ib, II
5 : 1	900	96	II
4 : 1	900	100	II, Bi_2WO_6
2 : 1	900	48	Bi_2WO_6
1 : 1	825	96	$Bi_2W_2O_9$

6 : 1, 4 : 1, 2 : 1, and 1 : 1. Bi_4WO_9 and $Bi_{12}WO_{21}$ were found to exist within the solid solution regions. In 1974, Hoda and Chang (15) observed four intermediate phases in the Bi_2O_3-WO_3 system: $Bi_{14}WO_{24}$, $Bi_{14}W_2O_{27}$, Bi_2WO_6, and $Bi_2W_2O_9$. The $Bi_{14}WO_{24}$ phase was tetragonal, with $a = 5.52$ and $c = 17.39$ Å. $Bi_{14}W_2O_{27}$ had a *fcc* structure and formed an extensive range of solid solutions with the unit cell parameter $a = 5.61$ Å.

In addition, Watanabe et al. (16) pointed out that the solid solution range based on $Bi_{14}W_2O_{27}$ in the Bi_2O_3-WO_3 system was limited between the composition with the WO_3 content of 21.3 and 26.3 mole% at 700°C. $Bi_{14}W_2O_{27}$ had a space group $I41/a$, with $a = 12.5143$ and $c = 11.2248$ Å. The structure was based on a defect fluorite substructure. For the Bi_6WO_{12} composition, Shuvaeva and Fesenko measured the cubic unit cell dimension $a = 11.182$ Å (17). Most of the literature on this system concentrated on Bi_2WO_6. Its structure was solved as an $n = 1$ member of the Aurivillius family (18).

Although, in a complex oxide system, different types of structures are usually produced depending on the preparation conditions, it should also be mentioned that almost all of the specimens in the Bi_2O_3-WO_3 system were polycrystallites and the structure determination was performed by using the powder XRD technique, which is believed to be too insensitive to detect superstructures in a solid solution material. In the present work, 12 different compositions in the Bi_2O_3-WO_3 system have been synthesized and their structures have been investigated by means of XRD and HREM. Similar to the Bi_2O_3-Nb_2O_5 system (3), the β-type and defect fluorite-related solid solutions with different superstructures were observed. These results are summarized and compared with those from previous work in Fig. 1.

EXPERIMENTAL

Stoichiometric mixtures of starting materials, Bi_2O_3 (99.9%) and WO_3 (99.99%), were weighted to an accuracy of ±0.1 mg. The specimen was prepared by grinding the mixture of oxides with acetone in an agate mortar and pestle for a few minutes; this mixture was then allowed to air-dry before being transferred to a silica boat, which was placed in a tubular furnace operating at the desired temperature. Pure oxygen with a flow rate of ca. 15–20 cm³/min at 1 atm was used during the sample preparation to avoid any possible reductions of the specimen. The sample was quenched directly to room temperature. Heating temperatures and initial preparation times for all compositions studied are listed in Table 1.

Initial characterization of the specimens was performed by XRD on a Philips diffractometer using Cu-$K\alpha$ radiation with operating conditions of 40 kV and 40 mA. Further identification of each phase was by selected area electron diffraction (SAED) and HREM. The electron microscope employed was a Jeol-200CX fitted with a LINK 860 energy-dispersive analytical (EDS) attachment which was used to determine the cation ratios in the samples. SAED patterns were recorded using a ±45° double tilting goniometer stage. This enabled us to take one set of SAED patterns from each microcrystal and, therefore, to deduce the unit cell and possible symmetries of the structure. HREM images were recorded on another Jeol-200CX electron microscope using an improved top entry goniometer system with electron optical parameters $C_s = 1.2$ mm and $C_c = 1.4$ mm, corresponding to a point resolution at optimum focus of 2.43 Å. Computer simulations of the SAED patterns and HREM images were carried out according to the multislice method (19, 20), using the CERIUS HRTEM program developed by Cambridge Molecular Design, Ltd.
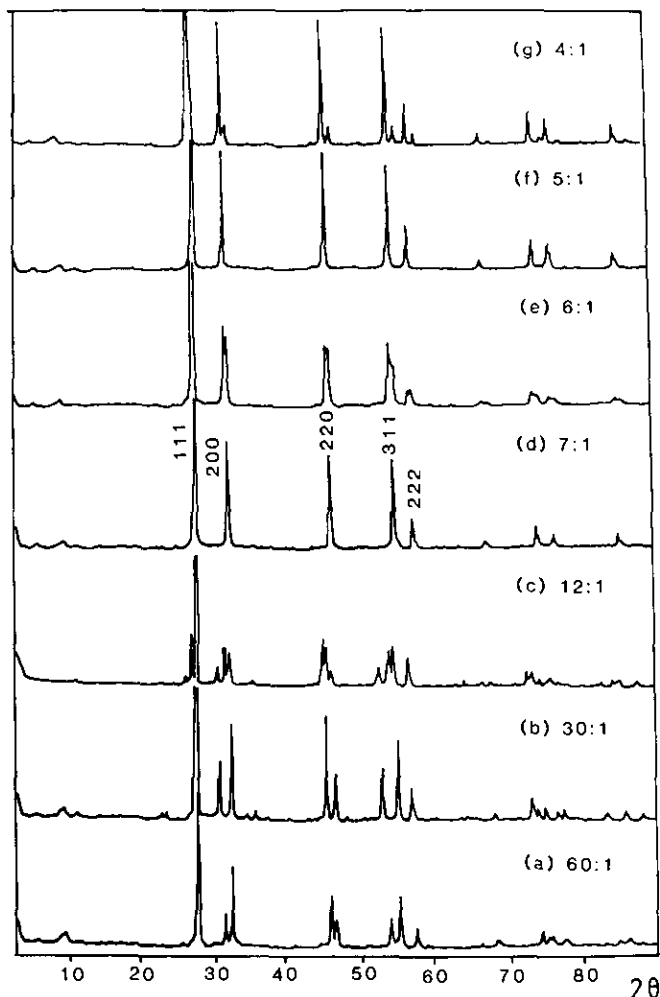
FIG. 2. XRD spectra of some compositions in the Bi₂O₃–WO₃ system. The ratios of cations, Bi : W, are indicated. That of 7 : 1 is indexed onto a δ-Bi₂O₃-like subunit cell.

RESULTS AND DISCUSSION

Homogeneities of the specimens were examined by EDS. Freshly prepared Bi_2WO_6, which is single phase, was used as a reference. The nominal composition of Bi_4WO_9 showed two phases in the EDS analysis. One was close to $Bi_{18}W_4O_{39}$ and the other was Bi_2WO_6. Both $Bi_{10}W_2O_{21}$ and $Bi_{14}W_2O_{27}$ were homogeneous. No evidence of impurities from Bi_6WO_{12} was detected in the EDS studies, despite a biphasic state indicated by the XRD pattern shown in Fig. 2e. For other Bi-rich specimens, the homogeneities could not be determined accurately by EDS. Therefore, XRD and SAED techniques became the alternatives.

XRD studies revealed the basic structure of each composition. Some of the spectra are shown in Fig. 2. All the XRD spectra in the compositional range from $Bi_{60}WO_{93}$ to $Bi_{14}WO_{24}$ can be indexed onto some fct subunit cells,

and the spectrum of the $Bi_{12}WO_{21}$ nominal composition indicated a two-phase assemblage of fct and fcc substructures (Fig. 2c). The XRD spectrum of $Bi_{18}W_2O_{33}$ is very similar to that of $Bi_{14}W_2O_{27}$. The latter and $Bi_{10}W_2O_{21}$ have cubic subunit cells with $a = 5.62$ and 5.58 Å, respectively, while Bi_6WO_{12} is a mixture of these two phases, as indicated by a slight split of all the diffraction peaks (Figs. 2d–2f). The main phase in Bi_4WO_9 is obviously the same as that in $Bi_{10}W_2O_{21}$ (Fig. 2g). A few extra weak diffraction peaks from Bi_4WO_9 indicate the formation of a second phase, which has been proved by SAED and EDS to be Bi_2WO_6.

The subunit cell parameters versus composition are shown in Fig. 3. From $Bi_{60}WO_{93}$ to $Bi_{12}WO_{21}$, parameter a of the tetragonal subunit cell is almost constant (about 5.52 Å), while parameter c increases from 5.66 to 5.79 Å when the composition changes from $Bi_{60}WO_{93}$ to $Bi_{30}WO_{48}$. The unit cell dimensions then present three flat stages in Fig. 3. The first one covers a compositional range from $Bi_{30}WO_{48}$ to $Bi_{12}WO_{21}$, having a tetragonal subunit cell with $a \approx 5.52$ and $c \approx 5.78$ Å. The second stage is from $Bi_{12}WO_{21}$ to Bi_6WO_{12}, where a cubic subunit cell with $a \approx 5.62$ Å has been observed. Finally, from Bi_6WO_{12} to Bi_4WO_9, the unit cell parameter, a, of another cubic subunit cell becomes ca. 5.57 Å.

According to a laser Raman study (I. E. Waches, unpublished work), the W cations in the specimens are in an octahedral coordination by oxygen. The mechanism of formation of the MO_6 octahedra inside the defect fluorite structure of δ-Bi₂O₃ by shifting oxygen atoms has been discussed in Ref. (3). Due to the different coordinations of oxygen for the W and Bi cations, when the WO_3 concentration is high enough, the W cations are more likely to form some special clusters inside the δ-Bi₂O₃ parent structure instead of existing in a random arrangement. This is the so-called "like with like" phenomenon in solid solution materials. As we expected, in the compositional
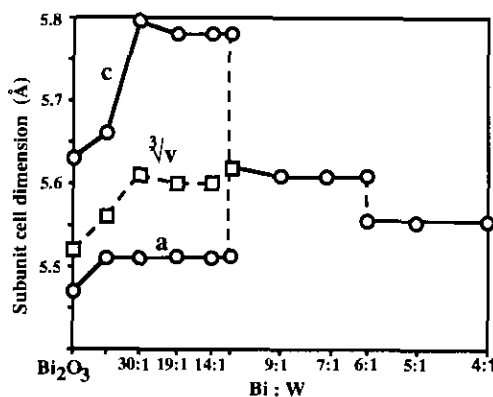

FIG. 3. Composition dependence of the subunit cell dimensions between Bi₂O₃ (β-type) and Bi₄WO₉.

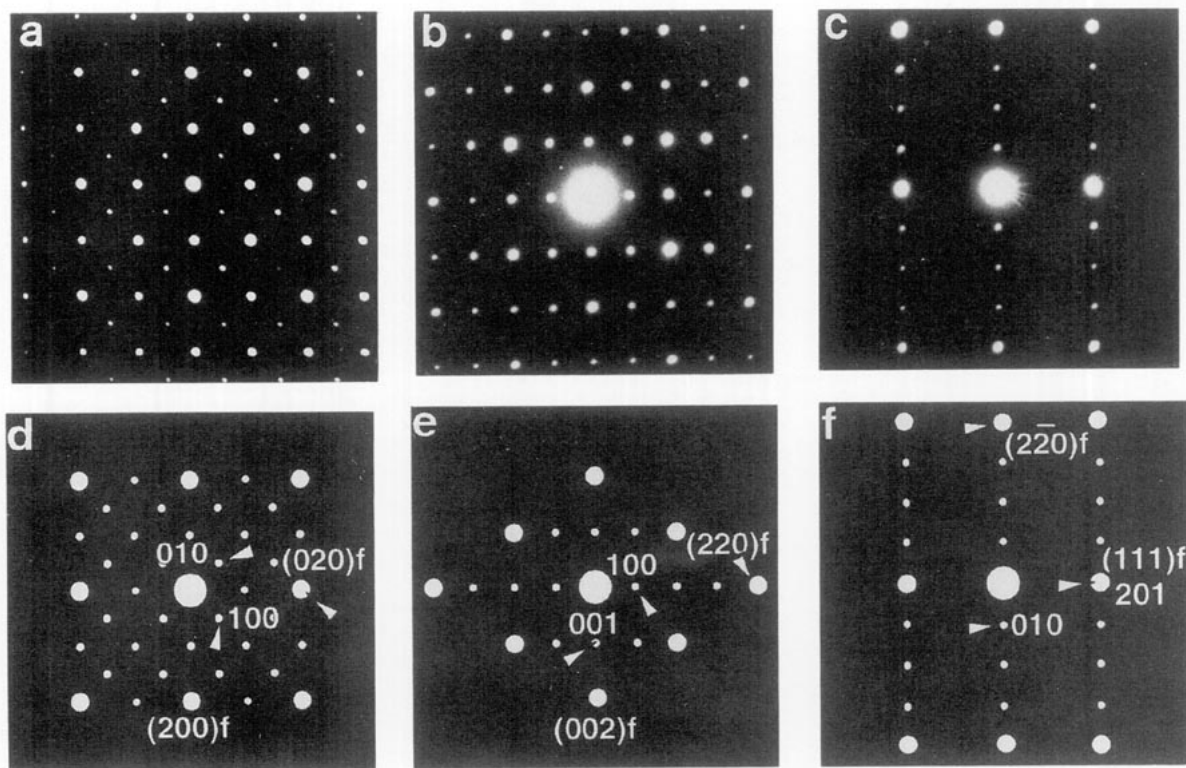FIG. 4. Observed SAED patterns from $Bi_{60}WO_{93}$ (a–c) and computer-simulated SAED patterns (d–f) from a model of β-Bi_2O_3 viewed down the [0 0 1] (a,d), [0 1 0] (b,e), and [1 0 $\overline{2}$] (c,f) zone axes. A specimen thickness of 100 Å was used in the calculations. The strong diffraction spots are indexed onto a β-Bi_2O_3-like subunit cell by $(hkl)_f$ and the weak spots are indexed onto the β-Bi_2O_3 unit cell by hkl.

range of the Bi_2O_3–WO_3 system investigated, HREM studies have revealed several superstructures derived from δ-Bi_2O_3. Each type of superstructure is discussed below.

β-Type Structure

Among the samples prepared, only $Bi_{60}WO_{93}$ has a β-Bi_2O_3-like structure, although the XRD spectra from $Bi_{60}WO_{93}$, $Bi_{30}WO_{48}$, $Bi_{38}W_2O_{63}$, and $Bi_{14}WO_{24}$ are all similar to each other (see Figs. 2a and 2b). Figure 4 shows three principal SAED patterns from $Bi_{60}WO_{93}$, viewed down the (a) [0 0 1], (b) [0 1 0], and (c) [1 0 $\overline{2}$] zone axes of the β-Bi_2O_3-like structure which has a tetragonal unit cell with lattice dimensions (a = 7.77 and c = 5.66 Å) slightly larger than those of pure β-Bi_2O_3 (a = 7.73 and c = 5.63 Å). Computer-simulated SAED patterns from a β-Bi_2O_3 structural model with zone axes corresponding to the observed ones (Figs. 4a–4c) are also shown in Figs. 4d–4f. These SAED patterns are very similar to those from the β-type solid solutions in the Bi_2O_3–Nb_2O_5 (3) and Bi_2O_3–Ta_2O_5 (5) systems, and the phase is likely to cover a narrow compositional range around $Bi_{60}WO_{93}$. No evidence of W ordering was found. In the β-Bi_2O_3 structure, each cation is coordinated by

six oxygen atoms [21], which is also favorable for the W cations.

As the content of WO_3 increased from $Bi_{60}WO_{93}$ to $Bi_{30}WO_{48}$, the unit cell dimension, a, remained the same and the c dimension significantly increased (Fig. 3). Therefore, the overall lattice dimension increased, although W^{6+} (0.62 Å) is much smaller than Bi^{3+} (0.96 Å). Actually the β-Bi_2O_3 structure can be regarded as a $\sqrt{2} \times \sqrt{2} \times 1$ superstructure derived from δ-Bi_2O_3, arising from atomic displacement near the oxygen vacancies. Excess oxygen introduced by WO_3 occupies some of the anion vacancies, consequently reducing the atomic displacement and increasing the unit cell dimensions. As one can see in the SAED patterns in Fig. 4, the strong diffraction spots can be indexed onto a distorted δ-Bi_2O_3-like subunit cell when viewed down the zone axes of (a) [0 0 1]$_f$, (b) [$\overline{1}$ 1 0]$_f$, and (c) [1 1 $\overline{2}$]$_f$. When the content of WO_3 increased, a phase transition from β- to δ-type took place. All the weak diffraction spots seen in Fig. 4 altered to form a new pattern, while the pattern of the strong spots was maintained (see the next subsection).

Since the phase transition from the β-type to the δ-type depends on a reduction of the oxygen vacancies, and WO_3 can bring relatively more oxygen anions into the structure,
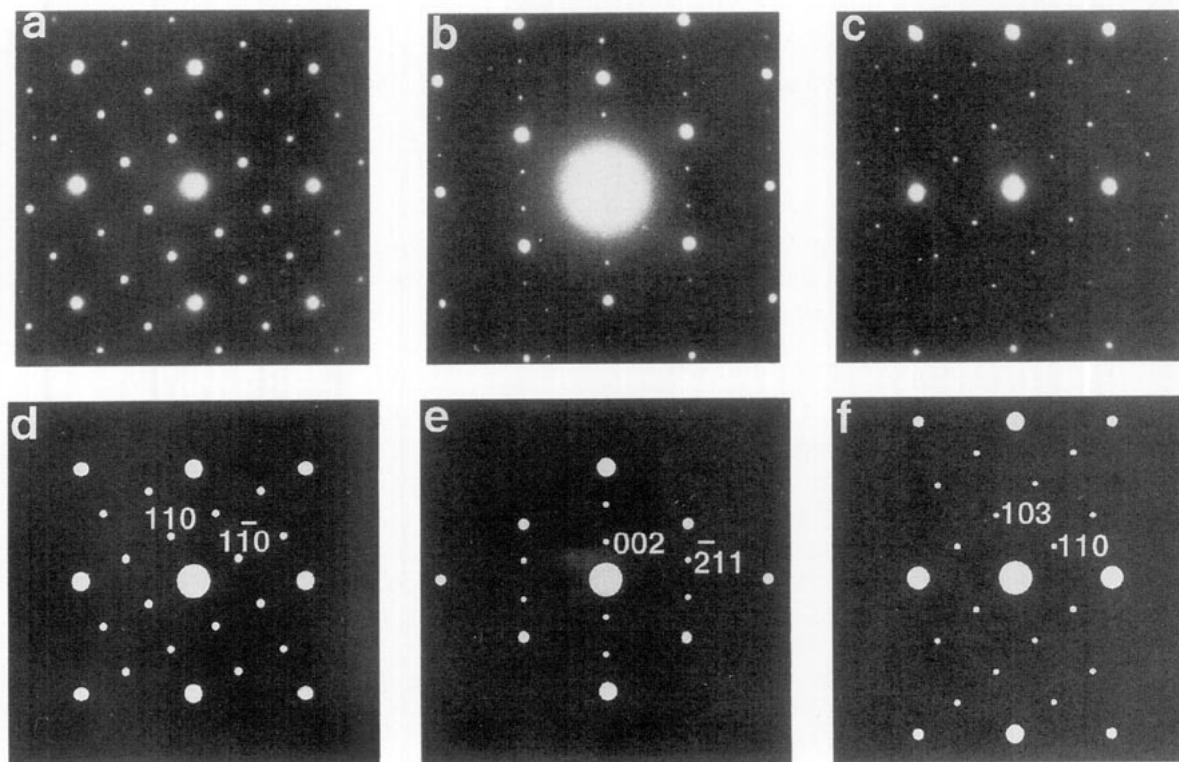
FIG. 5. Observed SAED patterns from $Bi_{30}WO_{48}$ (a–c) and computer-simulated SAED patterns (d–f) from the proposed model for the type Ia superstructure shown in Fig. 6, viewed down the [0 0 1] (a,d), [1 2 0] (b,e), and [3 3̄ 1̄] (c,f) zone axes. Specimen thicknesses of 200 (d), 400 (e), and 160 Å (f) were used in the calculations.

the compositional range of the β-type structure in the Bi_2O_3–WO_3 system is much narrower than those in the Bi_2O_3–Nb_2O_5 and Bi_2O_3–Ta_2O_5 systems. $Bi_{30}WO_{48}$ is clearly δ-Bi_2O_3-based without any similarity to β-Bi_2O_3 according to the SAED patterns presented in the next subsection. However, in the Bi_2O_3–Nb_2O_5 and Bi_2O_3–Ta_2O_5 systems, the δ-Bi_2O_3-related structures started to appear from the compositions of $Bi_{40}Nb_2O_{65}$ and $Bi_{25}TaO_{40}$, respectively.

The electron energy band gap, E_{bg}, of the specimens was measured by reflectance spectroscopy using a Perkin–Elmer Hitachi 200 spectrophotometer. The E_{bg} value of the WO_3-doped β-Bi_2O_3 is the lowest (2.28 eV) compared with the values (>2.5 eV) from other compositions in the Bi_2O_3–WO_3 system. It is believed that this physical property depends mainly on the degrees of lattice symmetries and densities of the solid solution materials. The nature of this property is assumed to be similar to that in the Bi_2O_3–Ta_2O_5 system and has been discussed earlier (5).

Type Ia Superstructure

Although the XRD spectra from all the compositions between $Bi_{60}WO_{93}$ and $Bi_{14}WO_{24}$ are similar, showing te-

tragonal substructures, the real structures in the compositions from $Bi_{30}WO_{48}$ to $Bi_{14}WO_{24}$ are related to δ-Bi_2O_3 instead of the β-type of $Bi_{60}WO_{93}$. Three principal SAED patterns obtained from $Bi_{30}WO_{48}$ are presented in Figs. 5a–5c. The substructural diffraction patterns formed by strong spots are the same as those in Figs. 4a–4c, also corresponding to the $[0\ 0\ 1]_f$, $[\bar{1}\ 1\ 0]_f$, and $[1\ 1\ \bar{2}]_f$ projections of the δ-Bi_2O_3-like subunit cell. However, the pattern of satellite diffraction spots has completely changed. The superstructure found in $Bi_{30}WO_{48}$, designated type Ia, has a *bct* unit cell with $a = 8.71$ and $c = 16.83$ Å. The relationship between the type Ia superunit cell and the distorted fluorite subunit cell can be described as

$$\mathbf{a}_{Ia} = 3/2\ \mathbf{a}_f - 1/2\mathbf{b}_f,$$

$$\mathbf{b}_{Ia} = 1/2\ \mathbf{a}_f + 3/2\ \mathbf{b}_f,$$

$$\mathbf{c}_{Ia} = 3\ \mathbf{c}_f,$$

where $\mathbf{a}$, $\mathbf{b}$, and $\mathbf{c}$ are unit cell vectors. The subscripts Ia and f indicate the type Ia superunit cell and the fluorite-like subunit cell. Accordingly, the projective directions of the SAED patterns in Fig. 5 are parallel to the (a)

[0 0 1], (b) [1 2 0], and (c) [3 $\bar{3}$ $\bar{1}$] zone axes of the type Ia superunit cell. The unit cell of $Bi_{14}WO_{24}$ determined by Hoda and Chang (15) (tetragonal with $a = 5.52$ and $c = 17.39$ Å) was probably related to $1 \times 1 \times 3$ superstructure derived from δ-Bi_2O_3. However, such a unit cell was not observed in the present work.

Almost all the SAED patterns of the type Ia superstructure from $Bi_{30}WO_{48}$ were also observed in the $Bi_{38}W_2O_{63}$ and $Bi_{14}WO_{24}$ compositions, indicating a solid solution state in this compositional range. The relative intensities of the satellite diffraction peaks were found to be variable, depending on the WO_3 concentrations.

It is believed that, similar to the type I superstructures in the other Bi_2O_3-containing ternary oxide systems (2–7), formation of the type Ia superstructure in the Bi_2O_3–WO_3 system is also mainly due to an ordering of the cations. The whole unit cell of the type Ia superstructure contains 30 cation sites and 60 anion sites. An ideal composition for the body-centered symmetry is $Bi_{28}W_2O_{48}$ with 12 oxygen vacancies, which is in agreement with the experimental results. $Bi_{14}WO_{24}$ was found to be single phase, with the type Ia superstructure. However, the nominal composition of $Bi_{12}WO_{21}$ contains a second phase detected in the XRD and SAED studies. Other compositions with the type Ia superstructure contain less W than $Bi_{14}WO_{24}$. Therefore, in these materials, the W cations only partially occupy the corner and body-centered positions in the superunit cell.

A structural model for the type Ia superstructure has been suggested as shown in Fig. 6. The model was initially built to be a $\sqrt{10}/2 \times \sqrt{10}/2 \times 3$ superstructure derived from the defect fluorite substructure of δ-Bi_2O_3, containing no oxygen vacancies and two Bi cations at the corner, and the body-centered positions were replaced by W cations. This model had a hypothetical composition of $Bi_{28}W_2O_{60}$ and a space group of $I4m$. The W cations were at $2a$ sites. The Bi cations were at $8h$ ($x = 2/5$, $y = 1/5$), $16i$ ($x = 2/5$, $y = 1/5$, $z = 1/3$), and $4e$ ($z = 1/3$) sites. Oxygen anions were at $4d$, $8g$ ($z = 1/12$), $16i$ ($x = 1/10$, $y = 4/5$, $z = 1/12$), $16i$ ($x = 3/5$, $y = 3/10$, $z = 1/12$), and $16i$ ($x = 1/5$, $y = 1/10$, $z = 1/4$) positions. However, such a model contained too many oxygen atoms and never generated satellite diffraction peaks of sufficient intensity in the computer-simulated SAED patterns. Twelve oxygen atoms were then removed from this model to match the right composition and to reduce the oxygen coordination from eight to six for the W cations. The positions of these removed oxygen atoms were at the (1/5, 1/10, 1/12), (4/5, 9/10, 11/12), (9/10, 1/5, 1/4), (1/2, 0, 5/12), (0, 1/2, 9/12), (1/10, 4/5, 7/12) sites and their body-centered equivalent positions. Using this model with correct oxidation states for the cations and correct oxygen coordination for the W cations, the computer sim-
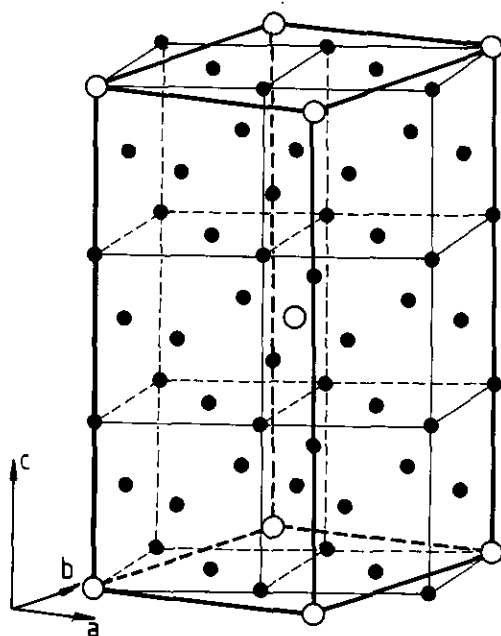

FIG. 6. A suggested model for the type Ia superstructure with an ideal composition of $Bi_{14}WO_{24}$. Only cations (solid circles for Bi^{3+} and open circles for W^{6+}) are shown. The cubes represent the fluorite-like sublattice.

ulation of the SAED patterns was successful, as seen in Figs. 5d–5f.

Because the content of WO_3 was so low, HREM images taken from the type Ia superstructure did not show sufficient contrast for the superstructure to be observed. Consequently, computer simulation of SAED patterns was the only technique used to determine the detailed structure. Due to the limited sensitivity of electron beam to light atoms, the cation positions in the proposed model (Fig. 6) are much more certain than the oxygen arrangement. Nevertheless, the model must be a better approximation of the real structure than those previously deduced from the XRD studies.

In the proposed model of the type Ia superstructure with the ideal composition of $Bi_{14}WO_{24}$, four oxygen vacancies are near neighbor to the two W cations and there are still eight anion vacancies located in the δ-Bi_2O_3 matrix. Therefore, it is possible to add more WO_3 to the materials without changing the isolated state of the WO_6 octahedra, which is the characteristic feature of the type I superstructure. In the present studies, the type I superstructure was maintained when the composition was beyond $Bi_{14}WO_{24}$, but the WO_6 octahedra were rearranged as discussed below in the type Ib superstructure.

Type Ib Superstructure

Two phases, type Ia and a new phase designated type Ib, were observed in the nominal composition of
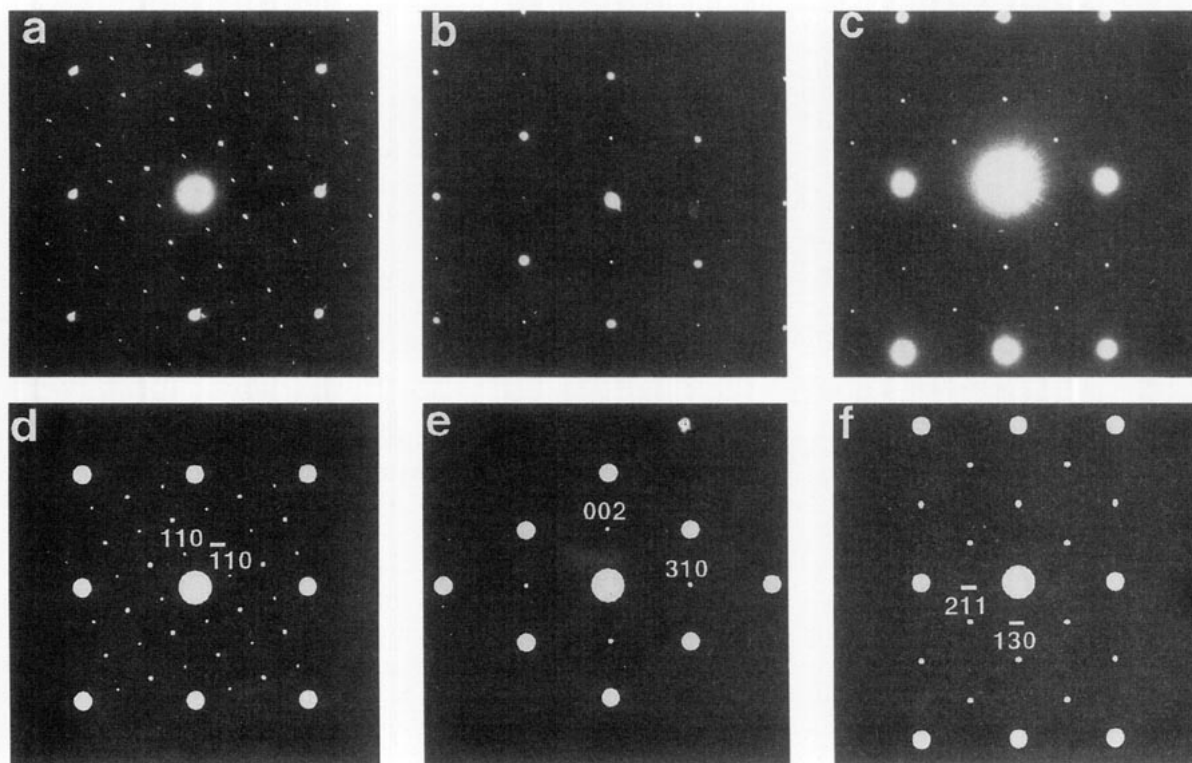
FIG. 7. Observed SAED patterns from $Bi_{14}W_2O_{27}$ (a–c) and computer-simulated SAED patterns (d–f) from the proposed model for the type Ib superstructure shown in Fig. 8, viewed down the [0 0 $\bar{1}$] (a,d), [1 $\bar{3}$ 0] (b,e), and [3 1 $\bar{5}$] (c,f) zone axes. Specimen thicknesses of 180 (d), 100 (e), and 140 Å (f) were used in the calculations.

$Bi_{12}WO_{21}$. The latter was the only phase found in $Bi_{18}W_2O_{33}$ and $Bi_{14}W_2O_{27}$. Although the type Ib superstructure has a cubic subunit cell indicated by the XRD spectrum (Fig. 2d), in agreement with the results reported by Hoda and Chang (15), a *bct* superunit cell with $a = b = 12.5$, and $c = 11.3$ Å has been revealed by the SAED studies. Figures 7a–7c show three SAED patterns from $Bi_{14}W_2O_{27}$, viewed down the zone axes of the δ-Bi_2O_3 subunit cell corresponding to those in Fig. 4 and Fig. 5 or the [0 0 1], [1 $\bar{3}$ 0], and [3 1 $\bar{5}$] zone axes of the type Ib superunit cell. Accordingly, the relationship between the superstructure and the δ-Bi_2O_3-like substructure is

$$a_{Ib} = 2 a_f + b_f,$$
$$b_{Ia} = -a_f + 2 b_f,$$
$$c_{Ib} = 2 c_f.$$

It has been noted that this unit cell is the same as that of $Bi_{14}W_2O_{27}$ previously reported by Watanabe *et al.* in 1985 (16). Using the XRD method, they determined the space group of the compound to be $I41/a$. Four W cations occupied the 4*a* sites, one W and three Bi cations shared the 4*b* sites, 32 Bi cations occupied two sets of the 16*f* sites, and all the oxygen anions were located at five sets of the 16*f* sites with an occupation factor of 84.4%. However,

using this structural model, none of the SAED patterns in Figs. 7a–7c were reproduced in the computer simulation. The satellite diffraction spots were too weak to be observed. It was noted that the XRD refinement performed by Watanabe *et al.* also gave some very low intensity superstructural diffraction peaks (about a few percent of the observed values) (16). The main disadvantage of Watanabe's model was that the locations of the oxygen vacancies were not considered. In the present work, the cation arrangement (Fig. 8) of Watanabe's model was used in the simulation of the SAED patterns. However, the coordination of oxygen for the W cations was reduced from eight to six to match the results from the laser Raman study. Body-centered symmetry was maintained, but the symmetry of the structure was lower than that of Watanabe's model. Using this model, the SAED patterns in Figs. 7a–7c have been reproduced by computer simulation (Figs. 7d–7f).

It is also noted that the solid solution range of this $\sqrt{5} \times \sqrt{5} \times 2$ superstructure determined by Watanabe *et al.* was from $Bi_{7.4}WO_{14.1}$ to $Bi_{5.6}WO_{11.4}$. However, in the present work, the range was found to be from $Bi_{24}W_2O_{33}$ to Bi_6WO_{12}. If we suppose that the principle of the type I superstructures in the systems Bi_2O_3–M_2O_5 (M = Nb, Ta, or V) (3, 5, 6) is also relevant to the Bi_2O_3–WO₃
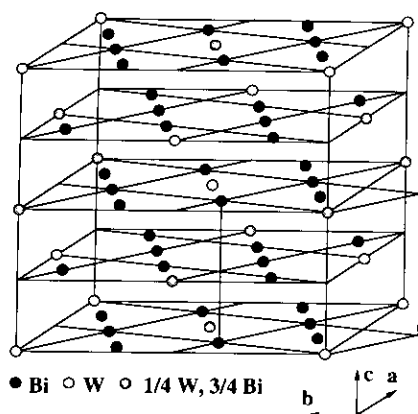
FIG. 8. A schematic drawing of the model for the type Ib superstructure with the composition of $Bi_{14}W_2O_{27}$. Only cations are shown. The small cube represents the fluorite-like sublattice.

● Bi   ○ W   ○ 1/4 W, 3/4 Bi

system, i.e., there is no bonding of W–O–W inside the structure, the general formula of the type I structure can be written as $Bi_{40-x}W_xO_{60+1.5x}$ with $20 - 1.5x$ oxygen vacancies. In the W upper-limit composition all anion vacancies are located around the W cations and each W cation freezes two anion vacancies, $x = 40/7$. The ratio of Bi : W is then 6 : 1, which is in good agreement with the present experimental results. In the nominal composition of Bi_6WO_{12}, the majority phase is still type Ib, with another phase starting to form, indicating that the real upper-limit composition of the type Ib superstructure is slightly Bi richer than Bi_6WO_{12}. In any case, a composition with W richer than Bi_6WO_{12} (e.g., $Bi_{5.6}WO_{11.4}$ as reported by Watanabe et al.) is unlikely to form the type Ib superstructure. In other words, the occupation factor for W on the sites shared by W and Bi cations in the type Ib model (Fig. 8) must be lower than 42.85%. It is then confirmed again that the structural type of these solid solution materials is controlled by oxygen vacancies, which is also the case in the $Bi_2O_3–V_2O_5$ system (6, 7).

The similarity of the cation arrangements in the W-containing (ab) planes of the type Ia (Fig. 6) and type Ib (Fig. 8) models is obvious. The main difference between these two superstructures is the periodicity of such W-doped (ab) planes along the c axes. When the W concentration increased, the distance between two W-doped (ab) planes decreased from three atomic layers to one atomic layer. The cation arrangement in the W-doped (ab) planes is much more stable than that in any other atomic planes inside the type I superstructures. A similar phenomenon was also found in the defect fluorite-related superstructures in the $Bi_2O_3–V_2O_5$ system, where a stable cation arrangement was found on one of the {1 1 1} planes of the δ-Bi_2O_3-like subunit cell. Variation of the distance between such (1 1 1) planes led to detection of several members of the type II superstructural family (6, 7). On

the other hand, the $2 \times 2 \times 2$ cubic type I superstructures discovered in the $Bi_2O_3–M_2O_5$ ($M=$ Nb or Ta) systems (3, 5) were never detected in the $Bi_2O_3–WO_3$ system.

To confirm the model for the type Ib superstructure, several HREM images have been obtained. Since the superunit cell axes, a_{Ib} and b_{Ib}, are not parallel to those of the fluorite subunit cell, a_f and b_f, most HREM images along the principal zone axes of the subunit cell gave very weak contrast information of the superstructure. On the other hand, when viewed down the main zone axes of the superstructure, the electron beam was not parallel to the principal axes of the subunit cell. Consequently, no atomic image was obtained due to the limit of the microscopic resolution. However, the superstructure should be visible along the c_{Ib} direction, which is parallel to c_f, on the HREM images. Figure 9 is a HREM image from $Bi_{14}W_2O_{27}$ viewed down the [1 $\bar{3}$ 0] zone axis of the type Ib superunit cell or the [1 1 0] direction of the δ-Bi_2O_3-like subunit cell. Twofold superlattice along the [0 0 1] direction is obvious. The image contrast can be reproduced (see the inset of Fig. 9) by computer simulation using the type Ib model shown in Fig. 8.

From most crystals, a large area of flat surface terminating with the (3 1 2)$_{Ib}$ or (1 1 1)$_f$ plane was observed. However, in some crystals, the (3 1 2)$_{Ib}$ surface was covered by a second phase (see the right bottom region of Fig. 9). The patterns of the dots in the bulk (type Ib) and the surface (second phase) areas are similar, both being related to the [1 1 0] projection of the δ-Bi_2O_3-like substructure. However, the subunit cell dimensions of the second phase are notably smaller (about 2%) than those of the bulk phase. Considering the composition dependence of the subunit cell dimensions (Fig. 3), the most probable phase which can match the d-spacings of the second phase in Fig. 9 is the W-doped β-Bi_2O_3. It is also noted that the image of the second phase presents relatively weaker contrast of any possibly existing superstructures. Consequently, it is assumed that the concentration of W in the surface area of the crystal observed in Fig. 9 is relatively lower than that in the bulk crystal. When the specimen was quenched at high temperature, this surface area could not maintain the δ-Bi_2O_3-like type Ia or type Ib superstructure. Alternatively, it transformed to a β-Bi_2O_3-like phase and intergrew with the type Ib bulk crystal. The interfaces of the intergrowth are the (3 1 2) plane of the type Ib and the (1 1 0) plane of the β-type. This is not surprising because these two planes are both (1 1 1) planes in terms of the δ-Bi_2O_3-like substructure.

Some complicated electron diffraction patterns from $Bi_7WO_{13.5}$ were also recorded. Figure 10a is a SAED pattern viewed down the [0 0 1] direction of the δ-Bi_2O_3-like substructure. The satellite diffraction maxima can be regarded as a combination of two simple electron diffraction patterns. One is viewed down the [0 0 1] zone axis
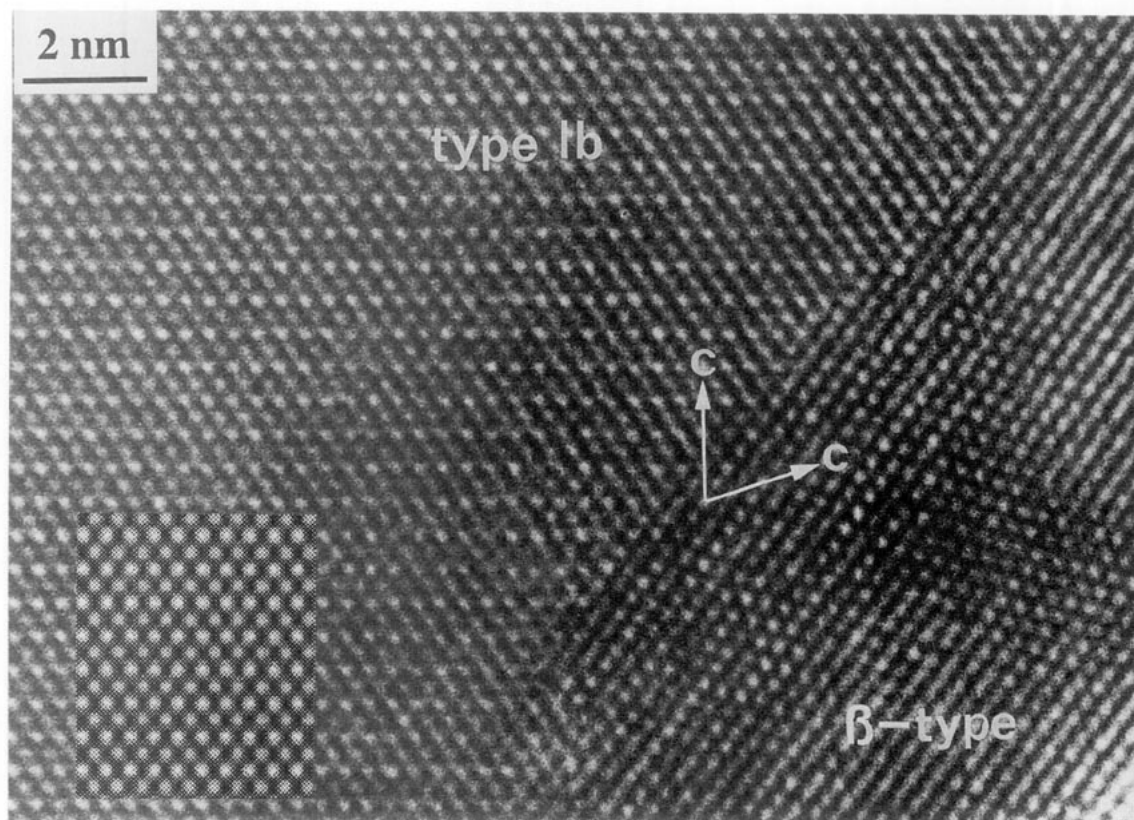
FIG. 9. HREM image from $Bi_{14}W_2O_{27}$, viewed down the [1 $\bar{3}$ 0] zone axis of the type Ib superstructure. The surface region (right) was identified to be β-Bi_2O_3-like solid-solution phase. The c axes of both phases are indicated. The inset is a computer-simulated image with 237.44 Å specimen thickness and −500 Å lens defocus from the proposed model for the type Ib structure shown in Fig. 8.

of the type Ia superstructure (Fig. 11a) and the other is viewed along the [1 2 0] direction of the type Ib superstructure (Fig. 11b). Figure 10b is also a [0 0 1] diffraction pattern from the δ-Bi_2O_3-like subunit cell. But here it presents four different satellite patterns, two [0 0 1] patterns of the type Ia superstructure with a twin angle of about 37.5° (Fig. 11c) and two [1 2 0] patterns of the type Ib superstructure with a twin angle of 90° (Fig. 11d). Figure 10c is a combination of three diffraction patterns when viewed down the [1 1 2] direction of the fluorite-like subunit cell, i.e., two [3 3 $\bar{1}$] (see Fig. 5f) patterns of the type Ia (Fig. 11e) and one [$\bar{1}$ 3 5] pattern of the type Ib (Fig. 11f) superstructures. The HREM images corresponding to these complicated SAED patterns reveal many domains in the crystals. For example, Fig. 10d is a HREM image corresponding to the SAED pattern in Fig. 10c. Intergrowth of two domains or a twin defect in the type I superstructure is visible, although the whole crystal is uniform in terms of the δ-Bi_2O_3-like substructure. It seems that, as the concentration of tungsten increased, the phase transformation from type Ia to type Ib took place in a single δ-Bi_2O_3-like crystal through rearrangement of the W cations. Figure 12a is a schematic

drawing of an intergrowth between type Ia and type Ib superstructures, from which the SAED pattern of Fig. 10a has been reproduced by computer simulation. Without the same δ-Bi_2O_3 matrix being shared, such intergrowth seems to be difficult. Figure 12b is another schematic representation of a twin defect in the type Ia superstructure viewed down the [0 0 1] direction, from which the SAED pattern shown in Fig. 11c has also been reproduced by the computer simulation technique.

As discussed above, in Bi_6WO_{12}, there are no anion vacancies in the δ-Bi_2O_3 matrix except those nearby the W cations. Although further substitution of Bi by W is still possible, the WO_6 octahedra must join to share anion vacancies in order to leave enough room to accommodate excess oxygen. Consequently, a further increase in the W concentration in Bi_6WO_{12} leads to formation of larger W–O clusters and, therefore, a completely new type of superstructure.

Type II Superstructure

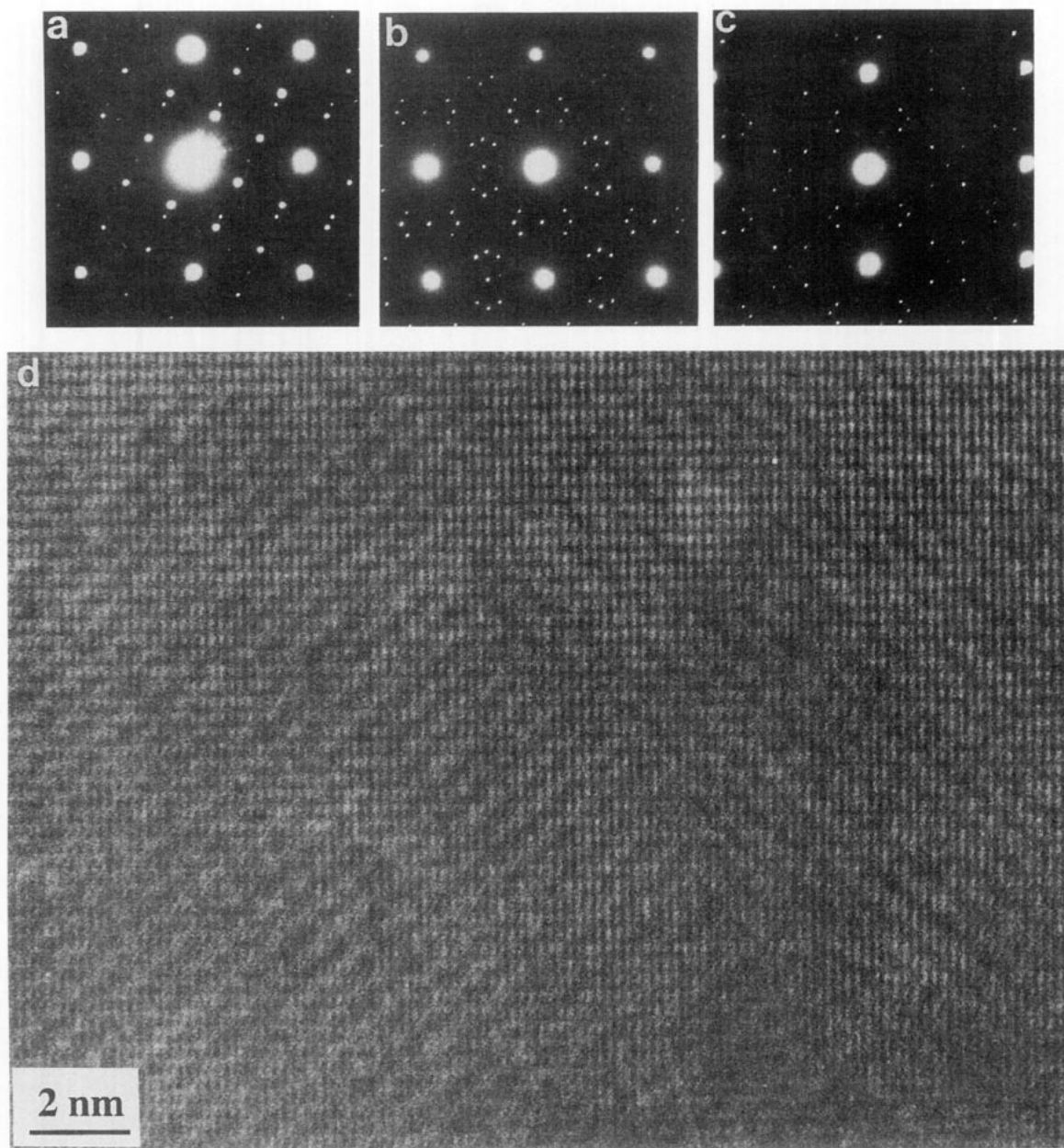The new phase appearing in the Bi_6WO_{12} nominal composition became the only phase in $Bi_{10}W_2O_{21}$ and had not

FIG. 10. SAED patterns from $Bi_7WO_{13.5}$, viewed down the [0 0 1] (a,b) and [1 1 2] (c) directions of the δ-Bi_2O_3-like subunit cell. (d) HREM image corresponding to (c) shows a twin defect in the type Ib superstructure.

only a fluorite-like substructure but also a cubic super-structure with a true three-fold repeat in all three dimensions. Some SAED patterns of this superstructure, designated type II, are shown in Figs. 13a–13c. Most of the satellite diffraction spots on these SAED patterns can be indexed onto a 3 × 3 × 3 face-centered superunit cell based on the fluorite-like subunit cell. However, there are some extra weak spots which depart from the face-centered symmetry. It is noted that these extra weak spots do not always appear on the SAED patterns. A reduction

of the symmetry in the structure is assumed to arise from a variation of the compositions.

One of the HREM images from Bi_4WO_9, when viewed down the [1 1 0] zone axis of the type II superunit cell, is shown in Fig. 14. The corresponding SAED pattern is shown in Fig. 13b. The [1 1 0] projection was the best for revealing the details of the superstructure rather than any other projections. The superunit cell dimensions and the pattern of image contrast are both similar to those of the type I superstructure of Bi_9VO_{16} (6). The diamond-shaped

(Fig. 10a)   (a)   (b)
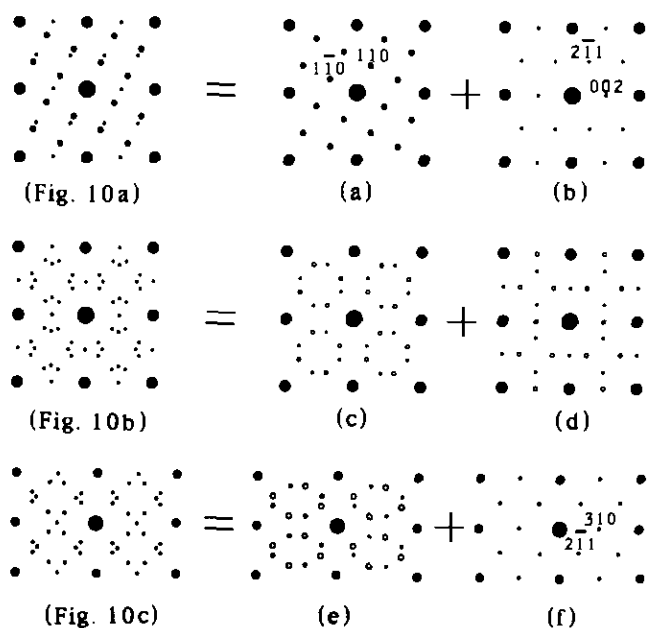
(Fig. 10b)   (c)   (d)

(Fig. 10c)   (e)   (f)

FIG. 11. Schematic drawings show the SAED patterns of Figs. 10a–10c combined with several simple electron-diffraction patterns from the type Ia and type Ib domains. (a) [0 0 1] pattern of type Ia, (b) [1 2 0] pattern of type Ib, (c) two [0 0 1] patterns of type Ia with a twin angle of about 37.5°, (d) two [1 2 0] patterns of type Ib with a twin angle of 90°, (e) two [3 3̄ 1̄] patterns of type Ia, (f) [1̄ 3 5̄] pattern of type Ib. Open and solid circles in (c), (d), and (e) represent two variants, respectively.

image contrast pattern indicates that the W cations must be arranged on the {1 1 1} planes of the 3 × 3 × 3 superunit cell rather than on the (0 0 1) planes as proposed for the type Ia and type Ib superstructures.

In Bi_9VO_{16}, all the V cations exist in isolated VO_4 tetrahedral units inside the δ-Bi_2O_3 parent structure. However, in the type II bismuth tungsten oxide, the WO_6 octahedra are no longer isolated due to the high concentration of WO_3. When two WO_6 octahedra share one oxygen anion and one anion vacancy, the oxygen arrangement in this W_2O_{11} cluster is able to accommodate two other WO_6 octahedra to form a W_4O_{18} tetrahedral unit (Fig. 15b) without further oxygen shift. Evidence of formation of clusters containing two or three guest cations were never observed in the Bi_2O_3–M_2O_5 (M = Nb, Ta, or V) systems nor in the Bi_2O_3–WO_3 system. M_4O_{18} seems to be a common form of cluster existing in these δ-Bi_2O_3-based mixed oxides. In this case, each cluster of four W cations in a unit of W_4O_{18} holds five oxygen vacancies instead of eight in the type I superstructures. Therefore, the material can dissolve more WO_3 and the fluorite-like structure is still maintained. Using this structural principle, a model for the type II superstructure with the composition of $Bi_{92}W_{16}O_{186}$ was suggested (Fig. 15a). The W_4O_{18} tetrahedral clusters (Fig. 15b) are located in the type II superunit cell and

obey a face-centered symmetry. All of these clusters then automatically lie on the {1 1 1} planes of the superunit cell. From this model, the observed SAED patterns shown in Figs. 13a–13c have been successfully reproduced (see Figs. 13d–13f). The image calculated from this model also matches the observed image very well in different regions of the crystal with different specimen thicknesses and lens defocuses (Fig. 14). Since the type II superstructure was found to cover a compositional range from Bi_6WO_{12} to $Bi_{4.5}WO_{9.75}$, the model shown in Fig. 15 is only an ideal. Variation of the number of the W_4O_{18} clusters in the type II superunit cell will certainly reduce the structural symmetry. Rotation of the W_4O_{18} clusters will also lead to a reduction of symmetry.

In the type II model, each W_4O_{18} cluster freezes five anion vacancies, and the formula of the type II material can be written as $Bi_{108-x}W_xO_{162+1.5x}$ with $54 - 1.5x$ oxygen vacancies. In the W upper-limit composition, with all anion vacancies around the W cations, $x = 19.64$. The
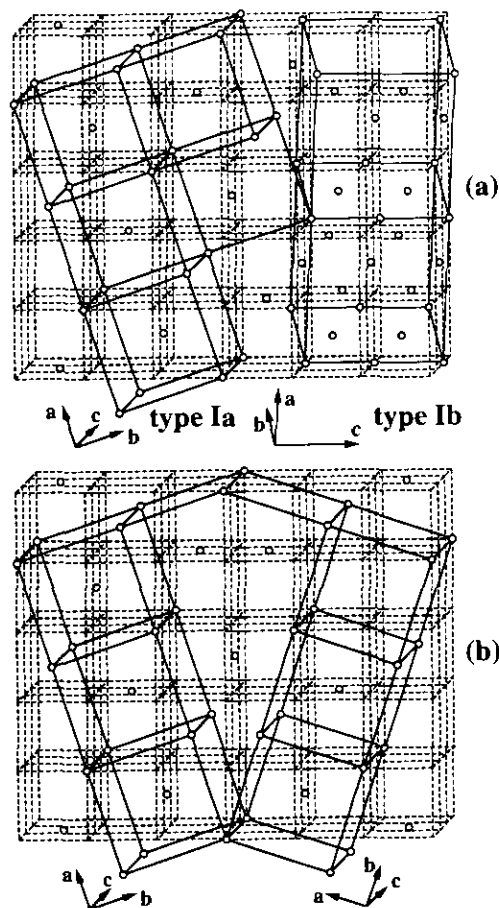

FIG. 12. Two schematic drawings of the models of intergrowth between type Ia and type Ib superstructures. Small cubes represent the fluorite-like sublattices. Solid lines show the superunit cells. Only W cations (open circles) are shown.
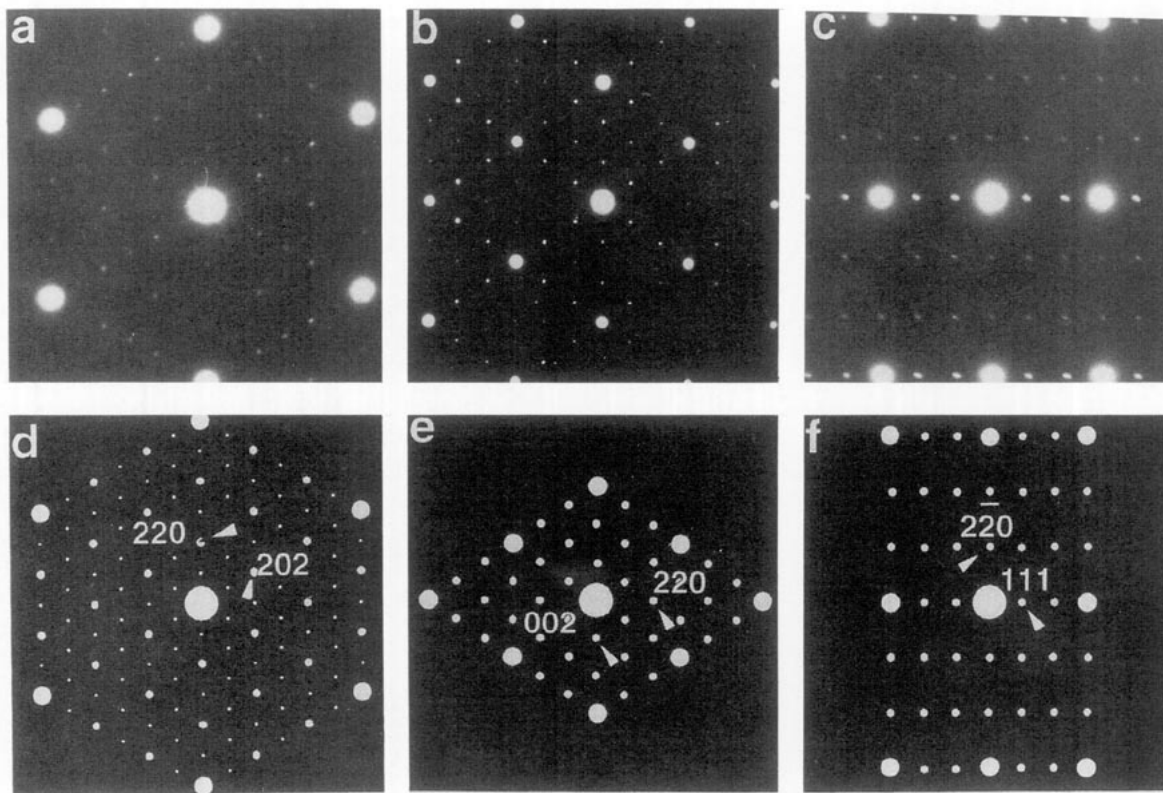
FIG. 13. Observed SAED patterns from Bi_4WO_9 along the (a) [1 1 1], (b) [1 1 0], and (c) [1 1 2] directions of the type II superstructure. (d–f) Corresponding SAED patterns reproduced by computer simulation using the model shown in Fig. 15. Specimen thicknesses of 170 (d), 200 (e), and 360 Å (f) were used in the calculations.

ratio of Bi : W is then 4.5 : 1, which agrees with the experimental observation that, in the $Bi_{10}W_2O_{21}$ composition, type II is the only phase found and that the specimen of Bi_4WO_9 contains two phases, $Bi_{4.5}WO_{9.75}$ (type II) and Bi_2WO_6 (Aurivillius phase). In the $Bi_2O_3–M_2O_5$ (M = Nb or Ta) system, the composition of the type II superstructure can extend at least up to $Bi_6M_2O_{17}$, because some larger clusters, M_7O_{30} and $M_{18}O_{72}$, can be formed (3, 5). Due to the relatively smaller cation size of W^{6+}, W_4O_{18} seems to be the only unit to exist inside the δ-Bi_2O_3 parent structure. According to the same reasoning, unlike the $Bi_2O_3–M_2O_5$ (M = Nb or Ta) system (4, 5), type III structures, in which the characteristic feature is a $M–O$ network made up of ordered intergrowths of the M_4O_{18} units and the perovskite-like M_4O_{20} square units, were not observed in the $Bi_2O_3–WO_3$ system. Further addition of WO_3 to $Bi_{4.5}WO_{9.75}$ led to an Aurivillius phase Bi_2WO_6 directly.

Bi_2WO_6 and $Bi_2W_2O_9$

Bi_2WO_6 is an n = 1 member of the Aurivillius family. The structure is made up of two components, Bi_2O_2 fluorite-like layers sandwiched by perovskite-like WO_4 sheets (Fig. 16a). $Bi_2W_2O_9$ is an n = 2 member of the Aurivillius

phases, with cation vacancies in the center position of the W_2O_7 perovskite blocks (Fig. 16b). Since there are no oxygen vacancies inside these two compounds, a substitution of Bi^{3+} in the Bi_2O_2 layer by W^{6+} is impossible.

In general, the Aurivillius family, $[Bi_2O_2][N_{n-1}M_nO_{3n+1}]$, includes a series of compounds with n from one to eight (22). The metal N, occupying the A sites of the perovskite blocks, could be Ca, Sr, Ba, Bi, Pb, Cd, La, Pr, Sm, Ho, Tb, Sc, Na, etc., and M, at the B sites, could be Nb, Ti, Ta, Fe, W, Cr, etc. It is very surprising that the Bi cations in the fluorite-like Bi_2O_2 layers in these compounds have no alternatives. Replacing the whole Bi_2O_2 layer by single- or double-cation layers leads to other classes of materials, which can be developed as high T_c superconductors by changing the electron count on the metals. However, all Aurivillius phases always seem to have a d^0 electron count on the metals. When one tries to reduce an Aurivillius phase by chemical substitution, the structure of the material can be easily rearranged to form various superstructures, intergrown compounds, or other members of the Aurivillius phases. Consequently, no valence fluctuation can be achieved (23). Since there are cation vacancies in $Bi_2W_2O_9$, partial reduction of W^{6+} by introducing metal atoms into these
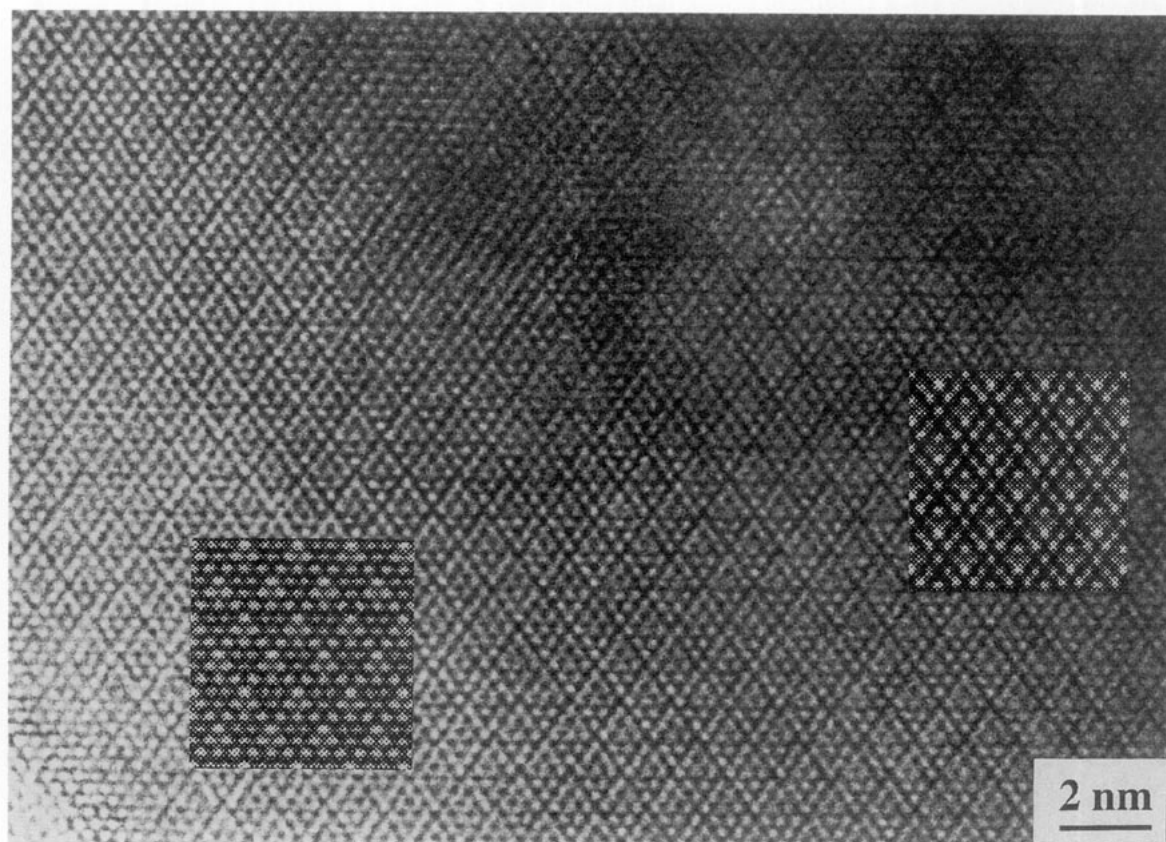
FIG. 14. HREM image of Bi_4WO_9, viewed down the [1 1 0] direction of the type II superunit cell. The insets are the simulated images calculated from a proposed model shown in Fig. 15. Specimen thicknesses are 93.34 (left) and 140.01 Å (right). Lens defocuses are -200 (left) and -800 Å (right).
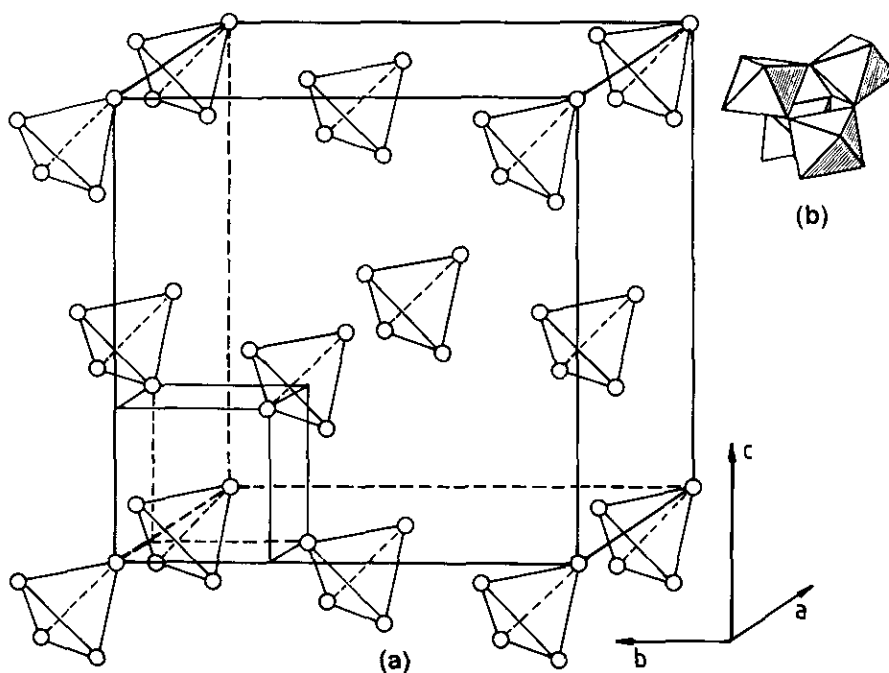

FIG. 15. (a) A structural model of the type II superstructure with the composition of $Bi_{92}W_{16}O_{186}$; only W cations are shown. (b) A W_4O_{18} tetrahedral unit in the type II superstructure.

cation vacancies becomes possible. Using a low-temperature technique (about 100°C), Rb and K metals have been successfully introduced into the structure of $Bi_2W_2O_9$. However, the materials were found to be air sensitive, immediately losing alkali metals in air (24). The structural properties of the Aurivillius phases are certainly related to the fluorite-like Bi_2O_2 layers.

In summary, the present work has extended the previous results obtained for the Bi_2O_3–WO_3 system. Four types of solid solutions have been identified in the compositional range from Bi_2O_3 to Bi_4WO_9 and their structures investigated by HREM. The structural type in the Bi_2O_3–WO_3 system was found to be governed by oxygen vacancies.

ACKNOWLEDGMENTS

FIG. 16. Schematic drawing of the structural models of (a) Bi_2WO_6 and (b) $Bi_2W_2O_9$.

REFERENCES

1. R. S. Roth and J. L. Waring, *J. Res. Natl. Bur. Stand, Sect. A* **66(6)**, 451 (1962).
2. W. Zhou, D. A. Jefferson, M. A. Alario-Franco, and J. M. Thomas, *J. Phys. Chem.* **91**, 512 (1987).
3. W. Zhou, D. A. Jefferson, and J. M. Thomas, *Proc. R. Soc. London, A* **406**, 173 (1986).
4. W. Zhou, D. A. Jefferson, and J. M. Thomas, *J. Solid State Chem.* **70**, 129 (1987).
5. W. Zhou, *J. Solid State Chem.* **101**, 1 (1992).
6. W. Zhou, *J. Solid State Chem.* **76**, 290 (1988).
7. W. Zhou, *J. Solid State Chem.* **87**, 44 (1990).
8. W. Zhou, D. A. Jefferson, and J. M. Thomas, Geophys. Monogr., Am. Geophys. Union **45**, 113 (1989).
9. A. Harriman, J. M. Thomas, W. Zhou, and D. A. Jefferson, *J. Solid State Chem.* **72**, 126 (1988).
10. A. V. Chadwick, W. Zhou, and J. M. Thomas, *Angew. Chem., Int. Ed. Engl.* **28(1)**, 75 (1989).
11. L. G. Sillen and K. Lundborg, *Ark. Kemi. Mineral. Geol.* **17A(21)**, 1, (1943).
12. N. P. Smolyaninov and I. N. Belyaev, *Zh. Neorgan. Khim.* **7**, 2591 (1962).
13. E. L. Gal'Perin, L. Ya. Erman, I. K. Kolchin, M. A. Belova, and K. S. Chemyshev, *Zh. Neorgan. Khim.* **11(9)**, 2125 (1966).
14. E. L. Speranskaya, *Izv. Akad. Nauk. SSSR. Neorg. Mater.* **6(1)**, 149 (1970).
15. S. N. Hoda and L. L. Chang, *J. Am. Ceram. Soc.* **57**, 323 (1974).
16. A. Watanabe, N. Ishizwa, and M. Kato, *J. Solid State Chem.* **60**, 252 (1985).
17. E. T. Shuvaeva and K. G. Fesenko, *Kristallografiya* **25(2)**, 408 (1980).
18. A. Ramanan, J. Gopalakrishenan, and C. N. R. Rao, *J. Solid State Chem.* **60**, 376 (1985).
19. J. M. Cowley and A. F. Moodie, *Acta. Crystallogr.* **10**, 609 (1957).
20. P. Goodman and A. F. Moodie, *Acta. Crystallogr. Sect. A* **30**, 280 (1974).
21. G. Gattow and D. Schutze, *Z. Anorg. Allg. Chem.* **328**, 44 (1964).
22. J. L. Hutchison, J. S. Anderson, and C. N. R. Rao, *Proc. R. Soc. Lond., A* **355**, 301 (1977).
23. W. Zhou, *Adv. Mater.* **2**, 94 (1990).
24. W. Zhou, P. A. Anderson, C. T. Lin and P. P. Edwards, *Physica C* **190**, 59 (1991).